ACS APPLIED MATERIALS & INTERFACES

Research Article

www.acsami.org

Aluminum Electrode Modulated Bipolar Resistive Switching of Al/Fuel-Assisted NiO_x/ITO Memory Devices Modeled with a Dual-Oxygen-Reservoir Structure

Kun-Keng Chiang,[†] Jen-Sue Chen,*[,‡] and Jih-Jen Wu*[,†]

[†]Department of Chemical Engineering and [‡]Department of Materials Science and Engineering, National Cheng Kung University, Tainan 701, Taiwan

Supporting Information

ABSTRACT: Bipolar resistive switching in Al/fuel-assisted NiO_x (40 nm)/ITO devices is demonstrated in this work. XPS analysis reveals the simultaneous presence of metallic Ni, Ni_2O_3, and NiO components in the fuel-assisted NiO_x. The concentration, as well as spreading of the metallic Ni and accompanying oxygen vacancies, are related to the Al/NiO_x interfacial reaction, which is enhanced by the increasing thickness of the Al top electrode. Correspondingly, the preswitching-on voltage decreases while the preswitching-off voltage increases with increasing thickness (from 15 to 60 nm) of Al. However, in regular switching operation, set and reset voltages are considerably lowered for devices with an increased thickness of the Al top electrode. The bipolar resistive switching behaviors of Al/fuel-assisted NiO_x/ITO devices are therefore discussed based on the formation of conductive paths and their correlation with the Al-electrode modulated composition in the fuel-assisted NiO_x. The Al/NiO_x interfacial reaction region pairs with ITO to form a dual-oxygen-reservoir structure. Mechanisms of construction/destruction of conducting paths originating from the electrochemical redox reactions at the interface between NiO_x, and the dual oxygen reservoirs will also be explicated.

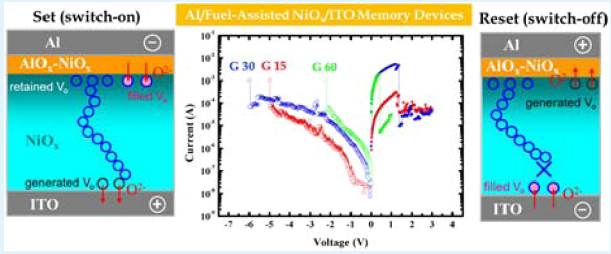

KEYWORDS: *bipolar resistive switching, Al electrode, fuel-assisted deposition, nickel oxide, interfacial reaction, oxygen reservoir*

INTRODUCTION

Resistance random access memories (RRAMs) of metal−insulator−metal (MIM) structure can be electrically switched between two nonvolatile resistance states, i.e., high resistance state (HRS) and low resistance state (LRS), by controlling the applied voltages to the devices.[1] Due to the simple device structure and nonvolatile characteristics, RRAMs have been widely investigated for potential application to nonvolatile memories with high-density integration, high speed, and low power consumption.[1−3] The resistive switching characteristics are observed in insulating materials such as transition metal oxides of NiO,[4−9] TiO_2,[8−10] WO_3,[11,12] and ZrO_2[13] with the MIM structures. The NiO thin film, which can be deposited by pulsed laser deposition,[4] reactive sputtering[5] and atomic layer deposition,[6] is one of the most investigated transition metal oxides for RRAM application. NiO usually possesses a unipolar resistive switching behavior, which is performed using the same bias polarity for set (switching from a HRS to a LRS) and reset (from a LRS to a HRS) operations.

The selection of electrode material is crucial to ensure reliable resistive switching properties of RRAM devices. For p-type NiO performing unipolar resistive switching behavior, an electrode which possesses the quasi-ohmic contact characteristic to NiO and an appropriate degree of blocking against oxygen ions, such as Pt, is suggested.[8] The selection of electrode materials is also crucial to realize the bipolar resistive switching characteristics of NiO, which have been demonstrated in only few papers.[14−18] Bipolar resistive switching can be performed on NiO devices with Pt/epi-NiO film/$SrRuO_3$,[14] $CaRuO_3$/epi-NiO film/$SrRuO_3$,[15] Ni/NiO film(thermally oxidized)/Ni[16,17] and Pt/Ni nanowire/Pt[18] structures.

On the other hand, aluminum is an inexpensive metal which possesses low resistivity and is compatible with the major processes in IC fabrication, making it a common interconnecting metal in microelectronic device fabrication. Al electrodes have also been employed to fabricate WO_x-,[12] TiO_2-,[19] TaO_x-[20] and graphene oxide-based[21] resistive memory devices. However, it has been reported that Al electrodes cannot drive either unipolar or bipolar resistive switching of NiO films due to the formation of a thin oxide layer at the interface between the Al electrode and NiO.[7,8,14]

In contrast to the literature, successful demonstration of bipolar resistive switching of fuel-assisted NiO film on indium tin oxide (ITO) substrate with an Al top electrode (Al/NiO_x/ITO) is achieved in this work. The fuel-assisted method has been reported to be an efficient chemical route for preparing

Received: May 27, 2012
Accepted: July 9, 2012
Published: July 9, 2012

   dx.doi.org/10.1021/am300946f | ACS Appl. Mater. Interfaces 2012, 4, 4237−4245

nanostructured metal oxide films.[12,22,23] The microstructure of the film can be easily tailored by the amount of fuel added in the precursor solution.[22] Moreover, the formation temperature of the crystalline oxide film can be significantly reduced by using an appropriate pair of fuel and oxidizer to ignite the exothermic reaction.[23] With the structure of Al/fuel-assisted NiO_x/ITO, the resistive switching behaviors of the device are strongly influenced by the thickness of the thermally evaporated Al electrode. This is attributed to the composition of the NiO active layer which is modulated by the interfacial reaction with the Al top electrode during Al evaporation. With the interfacial composition modulation, the bipolar resistive switching of the Al/fuel-assisted NiO_x/ITO devices can be accomplished based on the connection/rupture of conducting paths associated with the electrochemical redox reactions in a dual-oxygen-reservoir device structure. The characteristics, as well as the switching mechanism, of the preswitching and regular operation steps based on the model are delineated in this paper.

EXPERIMENTAL SECTION

Nickel oxide films were deposited on ITO substrates using a fuel-assisted method.[12,22] 5 mmol of nickel acetate hydrate (99%, Alfa Aesar) was dissolved into a mixture of 2.5 mL of hydrogen peroxide (30%, Sigma-Aldrich) and 2.5 mL of deionized water. Three mmol of glycine was then added into the solution followed by a 23 h aging period. The glycine-assisted nickel oxide films were deposited on ITO substrates (GemTech, 15 Ω/□) by spin coating. The films were then annealed at 450 °C for 30 min. The morphology of the nickel oxide films was examined using high-resolution field-emission scanning electron microscopy (SEM, PHI, XL-40FEG), while the crystal structures were investigated by field-emission transmission electron microscopy (TEM, JEOL JEM-2100F). Cross-sectional TEM samples were prepared using a focus ion beam (FIB, SEIKO, SMI 3050), and a thin Pt layer was deposited on the nickel oxide film to prevent charging. The compositions and chemical bonding states of the nickel oxide films were examined using X-ray photoelectron spectroscopy (XPS, PHI, 5000 VersaProbe).

To investigate the resistive switching behaviors of the glycine-assisted nickel oxide films, Al top electrodes of 220 μm × 220 μm with thicknesses of 15, 30, 60, and 100 nm were deposited on the NiOx films by thermal evaporation through a shadow mask to fabricate the Al/NiOx/ITO devices (named as G15, G30, G60 and G100 hereafter, respectively). A schematic of the Al/NiO_x/ITO device is shown in Figure 1. The device is characterized using a precision semiconductor parameter analyzer (Agilent 4156C) with a sweeping voltage applied to the Al top-electrode while the ITO bottom electrode was grounded. Current−voltage measurements were performed in a metal dark box to prevent disturbances from light and electromagnetic waves.

RESULTS AND DISCUSSION

Glycine is employed in this work as the fuel to assist in the formation of NiO_x films. Figures 2(a) and (b) respectively show the top-view and cross-sectional SEM images of glycine-assisted NiO_x film formed on an ITO substrate. The NiO_x film has a smooth surface with tiny pores and a thickness of ∼40 nm. A cross-sectional TEM bright-field (BF) image of the NiO_x/ITO sample is shown in Figure 2(c). The sample was covered with a surface Pt layer for TEM sample preparation to prevent the charging effect generated by the FIB thinning process. Figure 2(c) reveals that the glycine-assisted NiO_x film contains nanoparticles. In addition, lightly contrasted regions between grains suggest that pores or amorphous phase also exist within the NiO_x film. The granular-and-porous characteristic of the glycine-assisted NiO_x film is very different from the

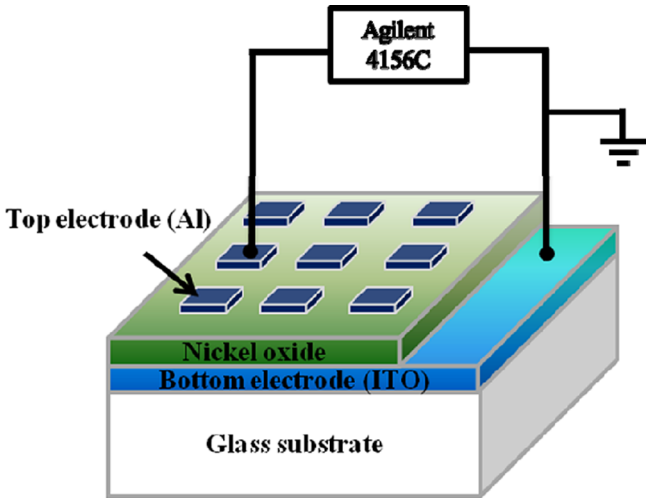

Figure 1. Schematic of Al/NiO_x/ITO devices and set up for measurement.

columnar-grain structure of the sputtering deposited NiO film.[24] A high-resolution TEM image and the corresponding selected area electron diffraction (SAED) of the NiO_x film are shown in Figure 2(d) and its inset, respectively. They reveal that the cubic NiO nanocrystals exist in the glycine-assisted NiO_x film.

Chemical bonding states of the glycine-assisted NiO_x film were characterized using depth-profiling XPS scans. Figure 3 displays the Ni $2p_{3/2}$ XPS spectra taken from a bare NiO_x film on an ITO substrate after sputtering etching for 0.1, 0.3, and 0.5 min. All XPS spectra are calibrated for the charging effect with reference to the C 1s peak at 284.5 eV.[25] Deconvolution curves of Ni $2p_{3/2}$ signals are also shown in Figure 3. The Ni $2p_{3/2}$ XPS scans are fitted by three Gaussian peaks centered at 852.7, 853.8, and 855.8 eV, pertaining to bonding states of Ni−Ni, Ni−O of NiO and Ni−O of Ni_2O_3, respectively.[25] XPS analysis on the NiO_x film indicates that the three components, including Ni, NiO and Ni_2O_3, are present in the glycine-assisted NiO_x film. The ratios of the three components estimated from the areas of the deconvoluted Ni $2p_{3/2}$ XPS peaks at different depths of the film are listed in Table 1, which reveals good depth uniformity on the bonding states of the glycine-assisted NiO_x film based on the relative precisions of ∼5% typically for quantitative analyses by XPS.[26] Since there is no crystalline metallic Ni or Ni_2O_3 phase observed by TEM diffraction, the metallic Ni and Ni_2O_3 components should exist in the amorphous matrix of the film. According to SEM, TEM and XPS results, we conclude that the glycine-assisted NiO_x film consists of nanocrystalline NiO embedded in a porous and amorphous matrix.

The resistive switching behaviors of the Al/NiO_x/ITO devices of different Al thicknesses are measured in sweeping current−voltage (I−V) mode with a compliance current of 10 mA to prevent the devices from permanent breakdown. For all three Al/NiO_x/ITO devices, a preswitching process was needed to attain the subsequent switching operation. Figure 4(a) shows the I−V characteristics of the preswitching processes for the G15, G30 and G60 devices. As shown in Figure 4(a), the pristine G15 and G30 devices initially exhibit HRS and are switched to LRS at threshold voltages of −1.9 V and −0.8 V, respectively, which is analogous to the electroforming step in some RRAM devices.[8] The preswitching process is then

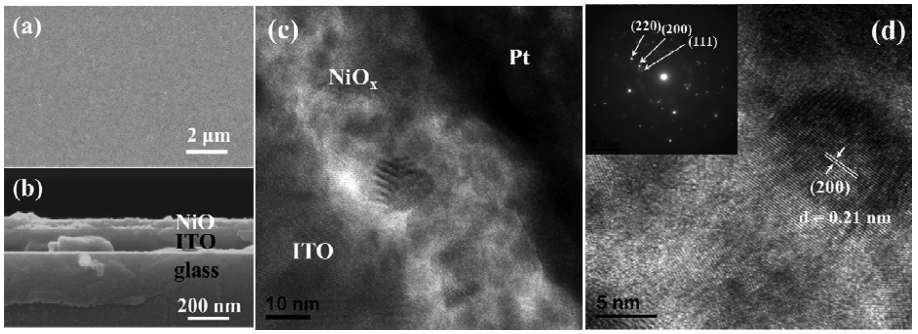

Figure 2. (a) Top-view and (b) cross-sectional SEM images of the glycine-assisted NiO_x film on an ITO substrate. (c) Cross-sectional TEM BF image of NiO_x/ITO. (d) HR TEM image and the corresponding SAED of the NiO_x film.

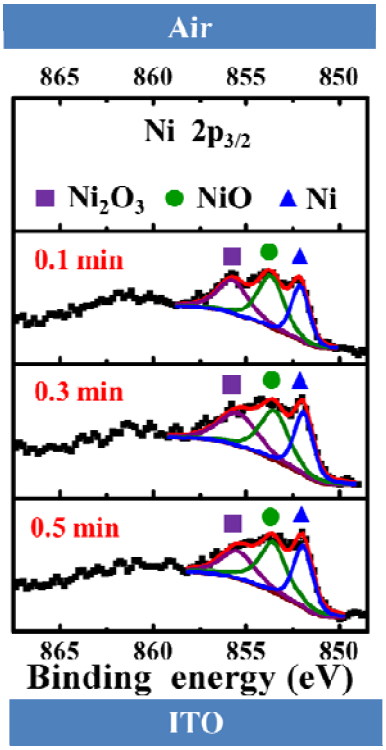

Figure 3. Ni $2p_{3/2}$ XPS spectra of bare NiO_x film on ITO substrate after various sputtering etching times.

Table 1. Ratios of the Ni, NiO, and Ni_2O_3 Components at Different Depths of Bare NiO_x Film[a]

sputtering time (min)	Ni (%)	NiO (%)	Ni_2O_3 (%)
0.1	27.4	40.2	32.4
0.3	30.0	37.4	32.6
0.5	31.5	42.0	26.5

[a]Data are estimated from the XPS results in Figure 3.

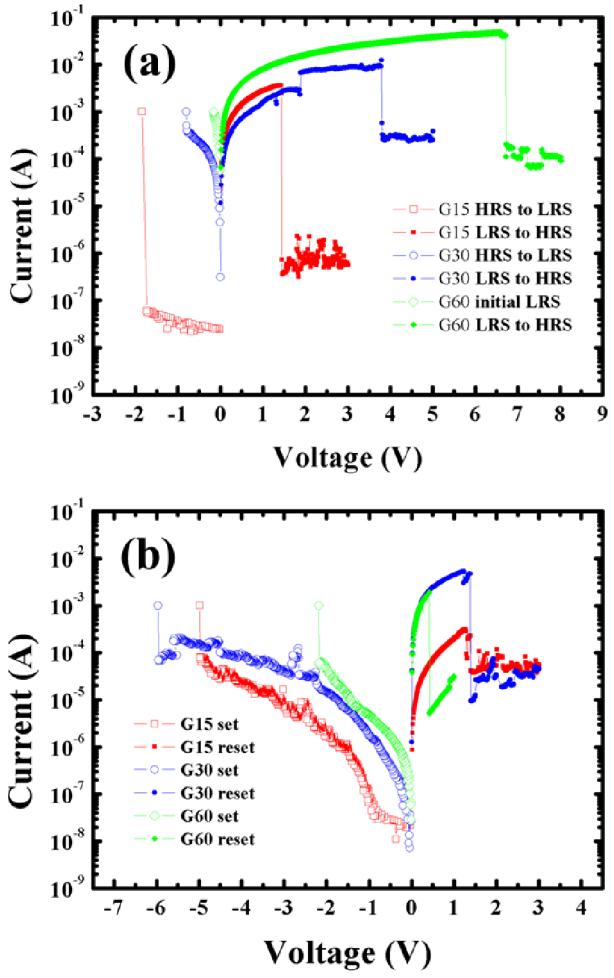

Figure 4. *I*−*V* characteristics pertaining to (a) preswitching processes and (b) regular switching operations for the G15, G30, and G60 devices, respectively.

completed by applying a positive bias sweep, where the G15 and G30 devices are switched back to HRS at threshold voltages of 1.4 and 3.8 V, respectively. On the other hand, the G60 device initially exhibits LRS and is able to be switched to HRS when applying a positive bias sweeping to a threshold voltage of 6.7 V, as shown in Figure 4(a). The preswitching process for the G60 is then complete.

For the subsequent regular switching operations, as shown in Figure 4(b), a set voltage of −5∼-6 V is applied on the G15 and G30 for switching HRS to LRS, while a reset voltage of 1−1.5 V is required for the opposite function. In the case of G60, the set and reset voltages are −2.3 and 0.5 V, respectively, which are significantly lower than those of the G15 and G30 devices. The results indicate that the three Al/NiO_x/ITO devices all perform the bipolar resistive switching behavior after an adequate preswitching operation. However, the threshold voltage in the preswitching process and the set/reset voltages in regular operations are dependent on the thickness of the Al top-electrode. The I−V measurement therefore indicates that the thickness of the Al electrode plays a crucial role in the resistive

dx.doi.org/10.1021/am300946f | ACS Appl. Mater. Interfaces 2012, 4, 4237−4245

switching behaviors of the Al/NiO_x/ITO devices. The unipolar resistive switching behavior of the G60 device was also investigated by applying the same voltage polarity for set and reset switching processes. Figures 5(a) and (b) reveal that the

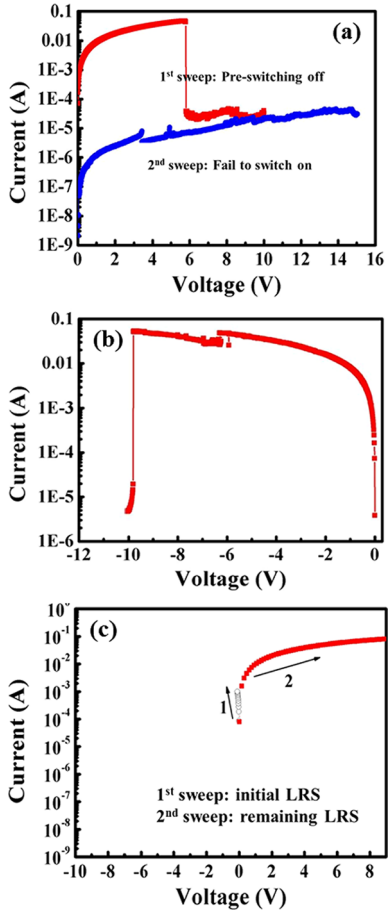

Figure 5. Unipolar *I*−*V* characteristics in the G60 device with applying (a) positive and (b) negative biases to the Al electrode, respectively. (c) *I*−*V* characteristics of the preswitching process in the G100 device.

unipolar resistive switching is not achievable in the Al/NiO_x/ITO device. Moreover, as shown in Figure 5(c), the G100 device, which initially exhibited a LRS as well, cannot be switched to HRS before the device is permanently destroyed by the high positive bias applied to the Al electrode.

The electrical stabilities of the Al/NiO_x/ITO devices at LRS and HRS have been examined using a retention test under a constant readout voltage of 0.1 V. As shown in Figure 6, both LRS and HRS of the G60 device are well maintained over 54000s, whereas the LRSs of the G15 and G30 devices only last for ∼40s and ∼13500s, respectively. This indicates that G15 is not fully qualified as an RRAM device due to its poor retention time. In addition, as shown in Figure 6(c), the current ratio of the HRS to LRS can be as high as $\sim 10^4$ in the G60 device. The results suggest that the Al/NiO_x/ITO device may possess superior nonvolatile characters of resistive switching if the thickness of the Al top electrode is optimally tailored.

To understand the resistive switching mechanism of the Al/NiO_x/ITO devices, depth-profiling XPS scans were conducted to investigate the effects of the Al top electrode thickness on the chemical states and composition of NiO_x. In terms of composition, depth-profiling XPS scans indicate that the device

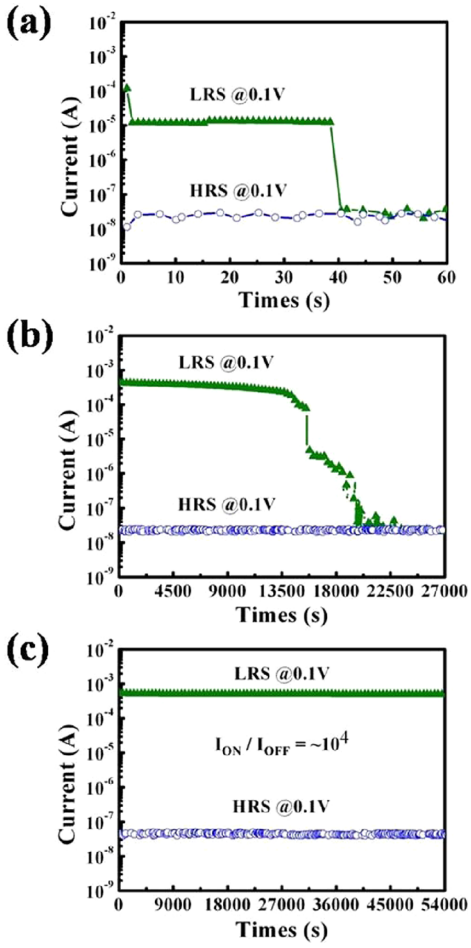

Figure 6. Retention tests for the LRS and HRS of (a) G15, (b) G30, and (c) G60 devices under a constant readout voltage of 0.1 V.

above the ITO electrode can be divided into Al-AlO_x, AlO_x-NiO_x and NiO_x regions. Here, the AlO_x- NiO_x region refers to the zone containing Al, Ni and O signals in the depth-profiling XPS scans, while the NiO_x region refers to the zone starting from the first layer without an Al signal until the layer before observing the In signal. Figure 7 shows XPS spectra and their Gaussian deconvolution fittings of the Al 2p signal in the Al-AlO_x and AlO_x-NiO_x regions and the Ni $2p_{3/2}$ signal in the AlO_x-NiO_x and NiO_x regions, taken from the three devices at various sputter-etching times. The Al 2p XPS scans are fitted by two Gaussian peaks centered at 72.9 and 74.7 eV, which correspond to the metallic Al−Al bonding and Al−O bonding of the Al_2O_3,[25] respectively. In addition, the area ratio of the Al−O component to Al−Al component increases with increasing sputtering times for all three devices, as shown in Figure 7, indicating that Al atoms mix with NiO_x at the interface between Al and NiO_x and capture O atoms from NiO_x to form AlO_x due to the lower free energy of formation for AlO_x than that for NiO_x.[27] The Ni $2p_{3/2}$ XPS scans are fitted with three peaks, including Ni−Ni and Ni−O of NiO, as well as Ni−O of Ni_2O_3, as shown in Figure 7. The ratios of the three components at various sputtering times (corresponding to different depths) are listed in Table 2. The concentrations of the Ni−Ni component in the AlO_x-NiO_x regions of the three devices are significantly higher in comparison with that in the bare NiO_x film shown in Table 1. This is consistent with the Al 2p scan showing that oxygen atoms of NiO_x are taken away by

dx.doi.org/10.1021/am300946f | ACS Appl. Mater. Interfaces 2012, 4, 4237−4245

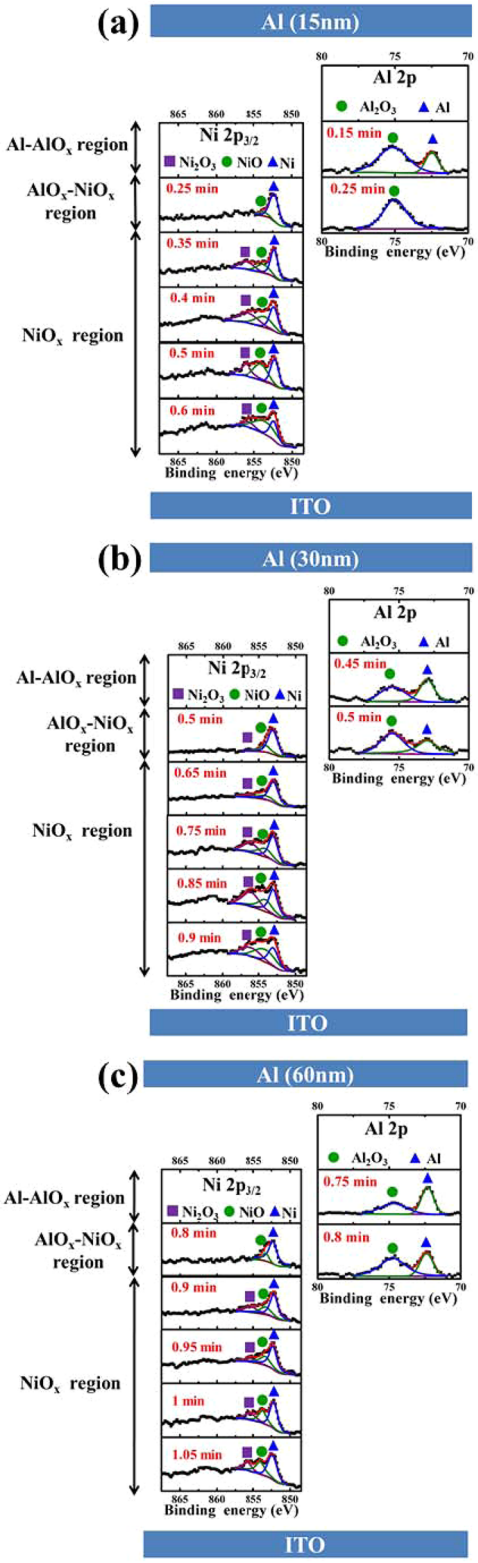

Figure 7. Ni $2p_{3/2}$ and Al 2p XPS spectra of (a) G15, (b) G30, and (c) G60 after various sputtering etching times.

Al atoms and metallic Ni is therefore formed in the AlO_x-NiO_x region. Moreover, the concentrations of the Ni−Ni component right below the AlO_x-NiO region (i.e., in the beginning of NiO_x region) of three devices are also higher than that in the bare NiO_x film and while the high Ni−Ni concentration section spans further with increasing thickness of the Al top electrode.

Table 2. Ratios of the Ni, NiO and Ni_2O_3 Components at Different Depths of the Three Al/NiO_x/ITO Devices. Data are Estimated from XPS Results in Figure 7

sputtering time (min)	region[a]	Ni (%)	NiO (%)	Ni_2O_3 (%)
		G15		
0.25	A	87.0	13.0	
0.35	B	48.9	25.5	25.6
0.4	B	35.6	31.5	32.9
0.5	B	35.7	35.7	28.6
0.6	B	33.1	54.4	12.5
		G30		
0.5	A	81.8	18.2	
0.65	B	63.4	24.6	12.0
0.75	B	38.5	31.9	29.6
0.85	B	39.0	27.7	33.3
0.9	B	34.1	37.4	28.5
		G60		
0.8	A	84.6	15.4	
0.9	B	52.3	26.1	21.6
0.95	B	55.6	32.1	12.3
1	B	52.0	29.0	19.0
1.05	B	51.5	23.9	24.6

[a]Region A: AlO_x-NiO_x ; B: NiO_x

XPS results indicate that the composition of the active layer of the Al/NiO_x/ITO device can be modulated via the degree of interfacial reaction between NiO_x and the Al top electrodes of different thicknesses.

With the presence of Al, oxygen atoms in NiO_x will diffuse toward and react with Al due to the existence of an oxygen concentration gradient and the high oxidation tendency of Al.[27] On the other hand, the two released electrons at the oxygen site will reduce the neighboring Ni^{2+} to generate metallic Ni, accompanied with the formation of one oxygen vacancy, in the NiO_x film. As a result, a high concentration of metallic Ni is observed in the Al/fuel-assisted NiO_x/ITO devices. The higher metallic Ni concentration observed from XPS analysis implies a greater concentration of oxygen vacancies in the NiO_x film. Therefore, as a sink of oxygen atoms, the thicker Al electrode in the G60 device leads to a wider extension of concentrated oxygen vacancy and metallic Ni region throughout the whole NiO_x layer in the G60 device. As a result, the pristine G60 device possesses a lower resistance than the G15 and G30 devices do.

Bipolar switching in oxide systems is generally related to the drift of oxygen ions. However, the resistance change may be attributed to construction/destruction of conducting paths via electrochemical redox reactions,[3] or related with the alteration in the interfacial Schottky barrier induced by the modulation of the oxygen-vacancy density.[1] In our system, because of the sharp current change at the set/reset processes (Figure 4), the bipolar resistive switching behaviors are explicated based on the arrangement of conducting paths via the electrochemical redox reactions in NiO_x.[2,17] The depth-profiling XPS scans of the pristine Al/NiO_x/ITO devices indicate that a highly concentrated metallic Ni component forms at the Al/NiO_x interfacial region (i.e., the AlO_x-NiO_x region), which can be regarded as an electrode in series with the Al top electrode. Moreover, founded on the concentration distribution of metallic Ni observed by XPS analysis (Table 2), the corresponding high-density oxygen vacancy networks extend into the NiO_x region,

dx.doi.org/10.1021/am300946f | ACS Appl. Mater. Interfaces 2012, 4, 4237−4245

and the extension is enlarged with increasing Al electrode thickness.

The origin switching mechanism of NiO memory devices (mostly unipolar switching) is still debatable. Park et al.[28] reported that the dc magnetron reactive sputtering deposited NiO film exhibited unipolar switching. Using EELS analysis, they concluded that conducting channels were formed by Ni atoms aggregated along the grain boundaries.[28] In the study done by *Oka et al.*,[18] the resistance switching of NiO nanowires was attributed to the gathering of Ni (cation) vacancies at the electrode interface. However, XPS analysis reveals that the fuel-assisted NiO_x layer is rich in metallic Ni, which should be associated with oxygen vacancies. We therefore attribute the formation of conducting channels to the line-up of oxygen (anion) vacancies.

In addition, most conventional bipolar switching devices are modeled with a sole oxygen reservoir, where oxygen exchanges at the interface between the active layer and one metal electrode.[29] The Al/NiO_x/ITO devices are first examined by the sole-oxygen-reservoir model as well, in which the ITO electrode performs as the oxygen reservoir.[30] The resistance change of the G60 device can be demonstrated by the sole-oxygen-reservoir model, i.e., the on/off switching is uniquely determined by the O^{2-} ions exchange at the NiO_x/ITO interface, which leads to the construction/rupture of conducting paths composed of oxygen vacancies. However, the sole-oxygen-reservoir model fails to explain the significantly greater switching-on voltages in the regular operation of the G30 and G15 devices, as compared to their preswitching on voltages (See Figure 4, and the details of which will be discussed later).

Therefore, we propose a dual-oxygen-reservoir structure to explain the electrical performances of the three Al/fuel-assisted NiO_x/ITO devices. Figure 8 shows the schematics of the Al/fuel-assisted NiO_x/ITO system and illustrates the electrochemical redox reactions at both top and bottom interfaces of NiO_x to facilitate the construction of conducting filaments. In this proposed scheme, both the AlO_x-NiO_x region and ITO electrode serve as the oxygen reservoirs to store and supply oxygen ions, depending on the polarity applied on the Al electrode. With oxygen reservoirs present at both top- and bottom-electrode interfaces, the construction of conducting paths may not be realized in the conventional MIM structure because there is always one terminal of the filament disconnected upon the filling of oxygen atoms at the vacancy sites under bipolar biasing. Nevertheless, for our Al/NiO_x/ITO devices, this dual-oxygen-reservoir structure will necessitate the success of bipolar resistive switching.

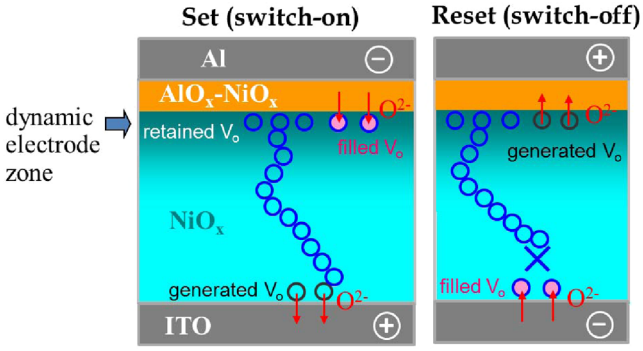

Figure 8. Schematics of electrochemical redox reactions at the top and bottom interfaces of the NiO_x layer. The AlO_x-NiO_x region and ITO both serve as oxygen reservoirs to form the dual-oxygen-reservoir structure. (Dimensions of individual regions are not to scale.)

When a negative bias is applied to the Al electrode, as shown in Figure 8, O^{2-} ions from the AlO_x-NiO_x region are driven toward the NiO_x region while the out-migrated O^{2-} ions oxidize NiO_x where parts of the oxygen vacancies are filled. However, some oxygen vacancies should be retained at the interfacial zone between the AlO_x-NiO_x and NiO_x regions since the metallic Ni content (correlated to the oxygen vacancy concentration) at the interface of the AlO_x-NiO_x and NiO_x regions is rather high, as shown in Table 2. With a sufficient amount of oxygen vacancies, this region is conductive and may act as a part of the top electrode. However, the quantity of oxygen vacancies at this interface is Al-thickness dependent as well as polarity dependent. Owing to its polarity-dependent characteristic, we name the interface as the "dynamic-electrode zone" hereafter. Simultaneously, with a negative bias applied to the Al electrode, the repulsive force drives O^{2-} ions to migrate to the ITO electrode, which also functions as an oxygen reservoir.[30] When an oxygen atom moves into the ITO electrode, an oxygen vacancy will be left behind in the NiO_x to generate the conducting path. Therefore, conducting paths in the NiO_x region can be constructed from the ITO electrode and extend to the dynamic-electrode zone by gradually lining up the newly generated oxygen vacancies at the NiO_x/ITO interface with the original vacancies already existing in the NiO_x under the electric field. This subsequently results in the formation of the conducting channels throughout the initially insulating NiO_x region, and the device is switched to LRS.

To reset the device, a positive bias applied to the Al electrode is required to switch LRS to HRS. As illustrated in Figure 8, O^{2-} ions in the device are driven toward the Al electrode under such an electric field. The numbers of oxygen vacancies in the dynamic-electrode zone would be increased when a positive bias is applied to the Al electrode due to the successful reduction of NiO_x by releasing oxygen to the reservoir of the AlO_x-NiO_x region. On the other hand, the conducting channels will be disconnected right above the ITO electrode because the O^{2-} ions are driven out from the oxygen supplier of the ITO electrode to fill the vacancy sites. Therefore, the device is switched to HRS. Accordingly, bipolar switching is achieved in the Al/fuel-assisted NiO_x/ITO system.

The detailed switching mechanisms for each individual device are shown in the Supporting Information and Figure S1. The electrochemical redox reactions at the NiO_x/oxygen reservoir interfaces govern the primary set/reset mechanism for all G15, G30 and G60 devices. The differences in switching characteristics among the three devices originate from the Al electrode thickness modulation effect. According to Table 2, increasing the Al thickness expands the distribution of metallic Ni, which also reflects the distribution of the associated oxygen vacancies. As shown in Figure S1 (Supporting Information), for the G15 and G30 devices, the network density of oxygen vacancies in NiO_x lessens gradually when approaching the ITO substrate. In contrast, in the pristine G60 device, the metallic Ni concentration, as well as the oxygen-vacancy concentration, remains almost equally high from top-electrode to bottom-electrode in the NiO_x layer. Hence, the G60 device exhibits a low resistance state whereas the G15 and G30 devices initially possess high resistance states. Concurrently, owing to its high oxygen vacancy concentration near the ITO, the G60 device

exhibits the largest preswitching off voltage because a significant amount of conducting channels need to be ruptured.

After the preswitching process, oxygen vacancies adjacent to the ITO are all filled, while the retained oxygen vacancies in the dynamic-electrode zone will still be substantial in the G60 but much fewer in G30 and G15 devices (as shown in Figure S1, Supporting Information). During the regular switching processes, the same effective electric field can be reached with a smaller applied voltage in the G60 device to drive the migration of oxygen ions because of its richer and wider spreading of oxygen vacancies (as shown in Figure S1, Supporting Information), which leads to a thinner poor-conductive region in the G60 device as compared to that of the G15/G30 devices. Consequently, the set/reset voltages of the G60 device are lower than that of the G15/G30 devices. Moreover, in the G30 and G15 devices, only few conducting channels remain in the dynamic-electrode zone after the preswitching-off step, and may be completely destroyed when the Al electrode is negatively biased and the O^{2-} ions are driven from the AlO_x-NiO_x reservoir to the dynamic-electrode zone. In the case of G30, a significantly higher set voltage (−6 V), as compared to its threshold set voltage (−0.8 V) in the preswitching process, is therefore required to redevelop the conducting channel from the ITO electrode to the AlO_x-NiO_x region. Here, the dual-oxygen-reservoir model successfully elucidates the fact that significantly greater switching-on voltages in regular operation of G30 and G15 devices are required as compared to their preswitching on voltages, which cannot be explained by the sole-oxygen-reservoir model.

Additionally, the unattainable unipolar resistive switching in the G60 device (Figure 5a, b) and the permanent LRS of the G100 device (Figure 5c) can also be explained by the dual-oxygen-reservoir model. As aforementioned, the preswitching process is completed when applying a positive bias to the Al electrode. The conducting channels, right above the ITO electrode, are disconnected due to O^{2-} ions migrating from the ITO electrode to NiO_x according to the electrochemical redox mechanism. The pristine G60 device is thus switched from the initial LRS to HRS. With the same polarity on the Al electrode, it is impossible to switch the G60 from HRS back to LRS because the direction of O^{2-} ion migration (from ITO toward Al) will not recover the disconnected conducting channel right above the ITO electrode. Therefore, switching of the highly resistive G60 back to LRS is not achievable despite the positive bias at the Al electrode sweeping to 15 V, as shown in Figure 5). On the other hand, when applying a negative bias to the Al electrode of a G60 device, the initial low-resistive G60 cannot be switched to HRS until a voltage of approximately −10 V is reached, as shown in Figure 5b. Under the bias polarity, O^{2-} ions migrate from the AlO_x-NiO_x region toward the ITO electrode, but the conducting channels right beneath the AlO_x-NiO_x region cannot be completely ruptured due to the existence of abundant oxygen vacancies. Instead, the ITO electrode is damaged at such a high voltage and the neighboring memory cells (with a common ITO electrode) are no more functional because their resistance of becomes exceedingly high. Moreover, Figure 5(c) shows that the pristine low-resistive G100 device cannot be switched to HRS at positive bias. Because of the high concentration of oxygen vacancies in the NiO_x region of the G100 device, it is unlikely to fully destroy the conducting channels above the ITO electrode via filling up the vacancy sites with oxygen. As a result, the G100 device shows no resistance bistability.

As discussed above, the set/reset voltages are well related with formation of conducting channels, which is governed by the concentration and distribution of oxygen vacancies in devices. Apparently, the resistances of individual devices shall also correlate with their concentration of oxygen vacancies. To examine the resistances of the three devices at HRS, the devices were cycled between HRS and LRS while currents at HRS are measured by applying a reading voltage of 0.1 V after every set/reset cycle, as shown in Figure 9. The statistical results show

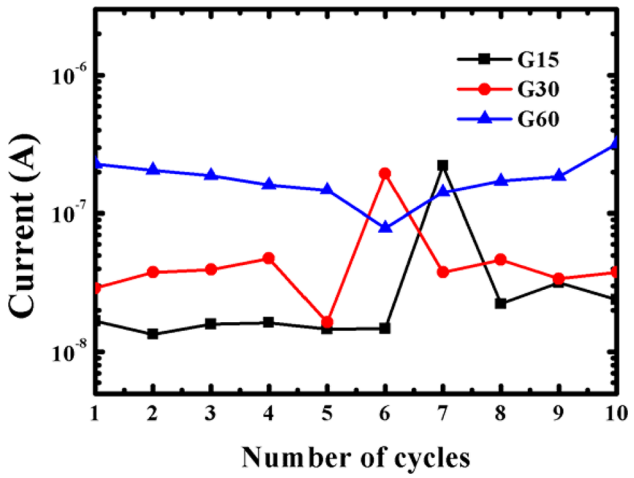

Figure 9. Currents of G15, G30 and G60 devices at HRS measured by applying a reading voltage of 0.1 V after every set/reset cycle.

that the currents at HRS of the Al/fuel-assisted NiO_x/ITO devices are in order of G15 < G30 < G60, which is consistent with the level of oxygen vacancy concentration of individual devices. However, the reason for the contradiction between the current level read at voltage greater than V_{reset} after reset process (shown in the positive voltage region of Figure 4) and the current level "read at 0.1 V" after reset process (shown in Figure 9) is still unknown. The difference in reading voltage (0.1 V vs greater than V_{reset}) may be the main cause but it is yet to be confirmed.

The shorter retention times in the G15 and G30 devices, as shown in Figure 6, are mainly attributed to the rupture of conducting channels due to thermal effect and the relatively low-density oxygen vacancies in those devices. The concentrations of oxygen vacancies in the pure NiO_x region of the devices decrease when reducing the Al thickness. When performing the retention test on the device at LRS, the thermal energy generated from the high current passing through the conducting channels will enhance the movement of oxygen vacancies as well as oxygen ions. Nearby the highest resistive points of the conducting channels, the oxygen vacancies might be filled by the thermally migrated oxygen ions.[31] If the concentration of oxygen vacancies is relatively low, such as in the G15 device, it may result in the rupture of the conducting channels because the concentration of oxygen vacancies is not sufficiently high to replace the intervening oxygen ions and reconnect the conducting channels. On the other hand, in the G60 device, the conducting channels are able to be sustained well when passing a high current through. This can be attributed to the high concentration of oxygen vacancies so that the vacancies will substitute the intervening oxygen ions easily. As a result, the conducting channels of G60 device at

LRS are able to be sustained well and the retention performance is excellent.

In this work, bipolar resistive switching of the fuel-assisted NiO_x film is successfully attained by using Al as the top electrode. This is contradictory to the literature data, where the Al electrode is not suitable for NiO-based RRAM devices due to the issues of the Schottky barrier[5] and interfacial oxide layer.[7,14] The successful implementation of the electrochemical redox mechanism for constructing conducting paths is ascribed to the presence of the AlO_x-NiO_x region and the dynamic-electrode zone. The AlO_x-NiO_x region works with the ITO electrode to form a dual-oxygen-reservoir structure, and also affects the quantity of oxygen vacancies in the underneath dynamic-electrode zone at different bias polarities. Formation of the AlO_x-NiO_x region is attributed to the distinctive granular-and-porous microstructure of the fuel-assisted NiO_x film (see Figure 2). With that, Al will expediently diffuse into and react with NiO_x to form a metallic Ni-rich AlO_x-NiO_x region. If the NiO_x is a vapor-deposited dense film, the Al/NiO_x interfacial reaction may only lead to a thin, stable and insulating AlO_x which prevents the resistive switching of NiO_x.[7,14] Additionally, the porous character of fuel-assisted NiO_x also facilitates the out-diffusion of oxygen to Al. As a result, the degree of the Al/NiO_x interfacial reaction can be simply modulated by varying the Al thickness during thermal evaporation. The dynamic-electrode zone of the G60 device contains sufficient oxygen vacancies, as compared to the G15 and G30 devices, to preserve conducting paths under various bias polarities, and will consequently govern the success of bipolar resistive switching in Al/fuel-assisted NiO_x/ITO devices. In addition to the memory cell application, because the set/reset voltages of Al/fuel-assisted NiO_x/ITO devices can be tuned by merely adjusting the Al electrode thickness, it would be promising to apply this character to construct a voltage-regulated current divider for controlling the current across individual circuit elements. The implementation has high potential because it can be expediently achieved by simply fabricating identical MIM (i.e., Al/fuel-assisted NiO_x/ITO) units with different Al electrode thicknesses.

CONCLUSIONS

An electrode-thickness dependent resistive switching behavior was demonstrated on a fuel-assisted solution-processed NiO_x active layer (40 nm), sandwiched between Al and ITO electrodes. The sharp resistance change and bipolar character of the Al/fuel-assisted NiO_x/ITO devices indicate a switching mechanism based on the conducting path construction associated with the electrical-bias-driven oxygen ion migration. XPS results reveal the formation of a metallic Ni-rich AlO_x-NiO_x region and the extension of metallic Ni into the NiO_x layer after the deposition of Al on the fuel-assisted NiO_x. The unique configuration originates from the distinctive granular-and-porous microstructure of the as-prepared fuel-assisted NiO_x film and high oxidation tendency of Al. By increasing the thickness of the Al top electrode, concentration and spreading of metallic Ni, as well as of the accompanied oxygen vacancies, increase and extend into the NiO_x layer. We suggest that the AlO_x-NiO_x region works with the ITO electrode to form a dual-oxygen-reservoir structure where the electrochemical redox reaction (i.e., the oxygen-vacancy exchange) occurs. Additionally, the AlO_x-NiO_x region is supplemented with an underneath dynamic-electrode zone. The formation of conducting paths in the dynamic-electrode zone is regulated via the oxygen vacancy population through the control of Al thickness and bias polarity. As a result, the set/reset voltages of Al/fuel-assisted NiO_x/ITO resistance memory devices are effectively modulated by the thickness of the Al electrode. This characteristic enables the Al/fuel-assisted NiO_x/ITO structure to not only be applied to memory cells but also provides the potential of serving as a voltage-regulated current divider by simply tailoring the thickness of the Al electrode.

ASSOCIATED CONTENT

Supporting Information

The detailed bipolar switching mechanisms for each individual device. This materials is available free of charge via the Internet at http://pubs.acs.org.

AUTHOR INFORMATION

Corresponding Author

*E-mail: jenschen@mail.ncku.edu.tw (J.-S.C.); wujj@mail.ncku.edu.tw (J.-J.W.).

Notes

The authors declare no competing financial interest.

ACKNOWLEDGMENTS

The authors gratefully acknowledge the financial support from the National Science Council of Taiwan (Grant No. NSC-101-3113-E-006-002 and NSC-100-2628-E-006-026-MY3).

REFERENCES

(1) Sawa, A. *Mater. Today* **2008**, *11*, 28−36.
(2) Waser, R.; Dittmann, R.; Staikov, G.; Szot, K. *Adv. Mater.* **2009**, *21*, 2632−2663.
(3) Waser, R.; Aono, M. *Nat. Mater.* **2007**, *6*, 833−840.
(4) Lee, S. R.; Char, K.; Kim, D. C.; Jung, R.; Seo, S.; Li, X. S.; Park, G.-S.; Yoo, I. K. *Appl. Phys. Lett.* **2007**, *91*, 202115.
(5) Seo, S.; Lee, M. J.; Kim, D. C.; Ahn, S. E.; Park, B.-H.; Kim, Y. S.; Yoo, I. K.; Byun, I. S.; Hwang, I. R.; Kim, S. H.; Kim, J.-S.; Choi, J. S.; Lee, J. H.; Jeon, S. H.; Hong, S. H.; Park, B. H. *Appl. Phys. Lett.* **2005**, *87*, 263507.
(6) You, Y.-H.; So, B.-S.; Hwang, J.-H.; Cho, W.; Lee, S. S.; Chung, T.-M.; Kim, C. G.; An, K.-S. *Appl. Phys. Lett.* **2006**, *89*, 222105.
(7) Lee, B.; Kang, B. S.; Benayad, A.; Lee, M. J.; Ahn, S.-E.; Kim, K. H.; Stefanovich, G.; Park, Y.; Yoo, I. K. *Appl. Phys. Lett.* **2008**, *93*, 042115.
(8) Choi, B. J.; Jeong, D. S.; Kim, S. K.; Rohde, C.; Choi, S.; Oh, J. H.; Kim, H. J.; Hwang, C. S.; Szot, K.; Waser, R.; Reichenberg, B.; Tiedke, S. J. *Appl. Phys.* **2005**, *98*, 033715.
(9) Kwon, D.-H.; Kim, K. M.; Jang, J. H.; Jeon, J. M.; Lee, M. H.; Kim, G. H.; Li, X.-S.; Park, G.-S.; Lee, B.; Han, S.; Kim, M.; Hwang, C. S. *Nature Nanotechnol.* **2010**, *5*, 148−153.
(10) Szot, K.; Rogala, M.; Speier, W.; Klusek, Z.; Besmehn, A.; Waser, R. *Nanotechnology* **2011**, *22*, 254001.
(11) Shang, S.; Shi, L.; Sun, J. R.; Shen, B. G.; Zhuge, F.; Li, R. W.; Zhao, Y. G. *Appl. Phys. Lett.* **2010**, *96*, 072103.
(12) Wu, W.-T.; Wu, J.-J.; Chen, J.-S. *ACS Appl. Mater. Interfaces* **2011**, *3*, 2616−2621.
(13) Lin, C. Y.; Wu, C. Y.; Wu, C. Y.; Lee, T. C.; Yang, F. L.; Hu, C.; Tseng, T. Y. *IEEE Electron Device Lett.* **2007**, *28*, 366−368.
(14) Lee, S. R.; Kim, H. M.; Bak, J. H.; Park, Y. D.; Char, K.; Park, H. W.; Kwon, D.-H.; Kim, M.; Kim, D.-C.; Seo, S.; Li, X.-S.; Park, G.-S.; Jung, R. *Jpn. J. Appl. Phys.* **2010**, *49*, 031102.
(15) Kim, H.; Lee, S.; Bak, J.; Jo, M.; Park, Y. D.; Char, K. *Jpn. J. Appl. Phys.* **2010**, *49*, 075801.
(16) Goux, L.; Lisoni, J. G.; Jurczak, M.; Wouters, D. J.; Courtade, L.; Muller, Ch. *J. Appl. Phys.* **2010**, *107*, 024512.

(17) Goux, L.; Polspoel, W.; Lisoni, J. G.; Chen, Y.-Y.; Pantisano, L.; Wang, X.-P.; Vandervorst, W.; Jurczak, M.; Wouters, D. J. *J. Electrochem. Soc.* **2010**, *157*, G187−G192.
(18) Oka, K.; Yanagida, T.; Nagashima, K.; Kanai, M.; Kawai, T.; Kim, J.-S.; Park, B. H. *J. Am. Chem. Soc.* **2011**, *133*, 12482−1485.
(19) Jeong, H. Y.; Lee, J. Y.; Choi, S.-Y. *Adv. Funct. Mater.* **2010**, *20*, 3912−3917.
(20) Zhang, L.; Huang, R.; Zhu, M.; Qin, S.; Kuang, Y.; Gao, D.; Shi, C.; Wang, Y. *IEEE Electron Device Lett.* **2010**, *31*, 966−968.
(21) Wang, L.-H.; Yang, W.; Sun, Q.-Q.; Zhou, P.; Lu, H.-L.; Ding, S.-J.; Zhang, D. W. *Appl. Phys. Lett.* **2012**, *100*, 063509.
(22) Wu, W.-T.; Liao, W.-P.; Chen, J.-S.; Wu, J.-J. *ChemPhysChem* **2010**, *11*, 3306−3312.
(23) Kim, M.-G.; Kanatzidis, M. G.; Facchetti, A.; Marks, T. J. *Nat. Mater.* **2011**, *10*, 382−388.
(24) Chen, H.-L.; Yang, Y.-S. *Thin Solid Films* **2008**, *516*, 5590−5596.
(25) Moulder, J. F.; Stickle, W. F.; Sobol, P. E.; Bomben, K. D. *Handbook of x-ray photoelectron spectroscopy*; Physical Electronic Inc.: Eden Prairie, MN, 1995.
(26) Skoog, D. A.; Holler, F. J.; Crouch, S. R. *Principles of Instrumental analysis*; Sixth ed., Thomson Brooks/Cole, Belmont, 2007, Ch. 21.
(27) Gaskell, D. R. *Introduction to the Thermodynamics of Materials*; Fourth ed., Taylor & Francis, New York, 2003, Ch. 12.
(28) Park, G.-S.; Li, X.-S.; Kim, D.-C.; Jung, R.-J.; Lee, M.-J.; Seo, S. *Appl. Phys. Lett.* **2007**, *91*, 222103.
(29) Akinaga, H.; Shima, H. *Proceedings IEEE* **2010**, *98*, 2237−2251.
(30) Chen, M.-C.; Chang, T.-C.; Huang, S.-Y.; Chen, S.-C.; Hu, C.-W.; Tsai, C.-T.; Sze, S. M. *Electrochem. Solid-State Lett.* **2010**, *13*, H191−H193.
(31) Lee, H. D.; Magyari-Kope, B.; Nishi, Y. *Phys. Rev. B* **2010**, *81*, 193202.